An Adjoint-state Full Waveform Tsunami Source Inversion Method and Its Application to the 2014 Chile-Iquique Tsunami Event

Tong Zhou[1], Lingsen Meng[2], Yuqing Xie[2] and Jiayuan Han[3]

[1]Department of Computational Mathematics, Science and Engineering, College of Engineering, Michigan State University
[2]School of Earth, Planetary and Space Sciences, University of California, Los Angeles
[3]Department of Earth, Environmental and Planetary Sciences, Rice University

Key Points:

- A new adjoint-state full waveform tsunami source inversion method is developed. The method is more computationally efficient than the traditional Greens-function-based inversions.
- The method does not rely on prescribed fault geometry to image earthquake-generated tsunamis, and has potential to resolve secondary tsunami sources such as seafloor landslide.

This article has been accepted for publication and undergone full peer review but has not been through the copyediting, typesetting, pagination and proofreading process which may lead to differences between this version and the Version of Record. Please cite this article as doi: 10.1029/2018JB016678

Corresponding author: Lingsen Meng, meng@epss.ucla.edu

Abstract

We develop an adjoint-state full waveform inversion procedure to recover the initial water elevation of a tsunami event. Traditional finite-fault tsunami source inversion methods suffer from the uncertainty of fault parameters or crustal rigidity. Moreover, the heavy computational burden of calculating Greens functions results in limited spatial resolution and hinders the real-time applicability of the traditional methods to tsunami early warning. In this work, we apply the adjoint-state full waveform inversion method to the tsunami source inversion. The benefits of the adjoint inversion are two folds: 1) independence of fault parameters, and 2) high computational efficiency, especially for dense tsunami arrays and high-resolution grids. We valid this approach with synthetic tsunami sources, and apply it to the 2014 Chile-Iquique tsunami event. Both synthetic and real-data results show that the adjoint-state method is of high efficiency and high resolution, outperforming the traditional tsunami source inversions.

1 Introduction

Tsunamis are oceanic gravity waves excited by the displacement of a large volume of water in the ocean, typically resulting from shallow megathrust earthquakes in subduction zones. Earthquake-generated tsunamis start as long-wavelength waves with relatively small amplitude in the open ocean, and become shorter and larger ($> 10\ m$) when shoaling near the coastlines, causing severe damage to coastal regions, home of over a third of the worlds population. Advances in the new tsunami monitoring instrumentation, including global Deep-ocean Assessment and Reporting of Tsunamis (DART, Satake (2014)) and coastal tide gauges provides an unprecedented volume of tsunami recordings. These observations enable numerous efforts to understand tsunami wave propagation and near-coast behaviors (Adriano et al., 2018; Fujii, Satake, Sakai, Shinohara, & Kanazawa, 2011; Maeda, Furumura, Sakai, & Shinohara, 2011; Satake, Fujii, Harada, & Namegaya, 2013), allowing tsunami warning systems and provide new opportunities to improve tsunami source imaging and probe the underlying physical mechanisms of tsunamigenic earthquakes.

Elevating the understanding of tsunami sources is crucial for both the tsunami early warning and the earthquake source studies. In 2011, the failure of accurate wave-height predictions of the M 9.0 Tohoku-Oki earthquake tsunami event caused large casualties because the tsunami run-up height was estimated less than 10 m but actually exceeding 30 m (Fujii et al., 2011). This failure was primarily caused by the underestimation of earthquake magnitude due to the satuation of magnitude estimation from early arrivals (Hoshiba & Ozaki, 2014). It is therefore important to explore the benefit of direct tsunami observations without relying on earthquake source models, which is crucial for constructing a better tsunami warning system.

Imaging the seafloor co-seismic deformation through tsunami source inversion provides crucial information on earthquake fault slip pattern, especially for shallow and near-trench slip distributions that are difficult to be well constrained by finite-fault inversions using teleseismic recordings and on-shore geodetic data. Instead, tsunami wave data are particularly sensitive to offshore ruptures and provide high spatial resolution for near-trench deformation (Satake et al., 2013). Recently, tsunami wave data have been directly adopted in the finite-fault slip models. An, Sepúlveda, and Liu (2014) inverted the tsunami data for the 2014 Chile-Iquique event; Yue et al. (2014) performed joint-inversion of seismic data, geodetic data and tsunami data for the 2011 Tohoku event. Both of these studies provide better constraints on the finite-fault model.

The two major applications of tsunami source imaging, call for different approaches to utilize the tsunami data, to solve for the initial water elevation for tsunami warning and to invert for the fault slip distribution for earthquake source studies, respectively. Initial water elevation inversion retrieves the tsunami water source directly, while the finite-fault model inversion requires the knowledge of the fault geometry and crustal rigidity. For many tsunami events without well-defined fault zone parameters, the finite-fault inversion is highly ill-posed and suffers from large model uncertainties. In contrast, initial water elevation inversion does not rely on the assumption of fault parameters and fault geometries (Hossen, Cummins, Roberts, & Allgeyer, 2015) and can potentially offer a stable and reliable constraint on the fault rupture processes. In addition to earthquakes, there are also other source mechanisms that cause seafloor deformations and generate tsunamis. Seafloor volcano eruptions and seafloor landslides are two common alternative tsunami sources. Seafloor landslides are sometimes triggered by submarine earthquakes, acting as secondary tsunami sources and increasing the amplitude of tsunami waves. Such second sources are suggested to explain the excessively large runup and inundation in Sanriku during the Tohoku earthquake (Grilli et al., 2013; MacInnes, Gusman, LeVeque, & Tanioka, 2013; Tappin et al., 2014). The initial water elevation inversion is also important for tsunami warning, because it takes into account all the tsunami sources, including seafloor landslides that cannot be well represented in the finite-fault modeling. It can also circumvents the issue of underestimating earthquake magnitude, and produces more accurate on-shore wave height estimation than seismic-based tsunami warning methods.

Several numerical methods have been applied to image the initial water source and associated seafloor deformation. The traditional linear inversion method divides the source region into small grids, and requires the calculation of the Greens functions between each pair of sources and receivers. This calculation is rather time-consuming because separate forward tsunami-wave simulations must be repeated many times. Time reversal imaging (TRI) is another popular method to image tsunami sources. According to acoustic theory, if the recorded data are dense and cover all azimuths, the reverse-propagated wavefronts focus at the source region at the occurrence time based on reciprocity principle. TRI has been applied in both exploration seismology (Nakata & Beroza, 2016; Sun, Xue, Zhu, Fomel, & Nakata, 2016), global seismology (Larmat et al., 2006), and tsunami research (Hossen, Cummins, Roberts, & Allgeyer, 2015). TRI excludes the smoothing regularization required by the finite-fault inversions and initial water elevation inversions (An et al., 2014; Fujii et al., 2011; Gusman et al., 2015; Heidarzadeh, Harada, Satake, Ishibe, & Gusman, 2016; Lay, Yue, Brodsky, & An, 2014; Satake, 2014; Wei, Chamberlin, Titov, Tang, & Bernard, 2013; Yagi et al., 2014), and also saves significant computational cost because the wave propagation simulation only needs to be conducted once. However, TRI only maps the region of the tsunami source but does not obtain the true initial water elevation. It also tends to introduce artifacts when the receivers are sparse or have poor azimuthal coverage. To mitigate the artifacts caused by the sparse data coverage and retrieve the true amplitude information, researchers have developed various techniques. In Hossen, Cummins, Dettmer, and Baba (2015), the TRI amplitude at a single source grid was corrected by the Greens functions from the source grid to receivers, known as GFTRI (Green's function-based time reverse imaging). Hossen, Gusman, Satake, and Cummins (2018) also derived a new adjoint-sensitivity analysis method, which removes the highly sensitive stations from the GFTRI imaging, and improves the robustness of the tsunami source inversion. These approaches make the TRI image feasible for further tsunami numerical modeling and fault slip inversions, although the calculation of the Greens Function weighting is still time consuming. In our previous work, An and Meng (2017) derived a much simpler and faster TRI approach with a unique station weighting method, which accounts for both 2D geometric spreading and azimuthal incompleteness. However, weighted TRI images still suffer from the incorrect amplitude and the artifacts due to the unevenly distributed stations, which limits the further usage of TRI images, for example, serving as an input of tsunami simulations. Using similar reciprocity principle of Green's function explored in TRI imaging, recently a two-step adaptive tsunami source inversion method (Mulia, Gusman, Jakir Hossen, & Satake, 2018) reduces the computational cost of high-resolution inversions.

In this project, we introduce a new adjoint-state method for tsunami source imaging. The adjoint method was used in oceanic and atmospheric data assimilation (Moore, 1991). We adopt the idea of adjoint full waveform inversion (FWI) in exploration seismology, and solve for the initial water elevation of tsunami events utilizing the adjoint wavefield. According to the Born approximation, the adjoint wavefield calculated by back-propagating the residue between data and model prediction is the gradient of the misfit function (Plessix, 2006). The least-square problem of waveform fitting is solved with a conjugate gradient method. Extensive synthetic tests conducted in exploration geophysics show that the adjoint-state method improves the resolution and balances the spatially unevenly distributed recordings (Feng & Schuster, 2017; Sun et al., 2016; Virieux & Operto, 2009) by taking advantage of the rich information embedded in the full wave field. This method is widely used in subsurface structure tomography, and is recently applied to earthquake source imaging (Somala, Ampuero, & Lapusta, 2018).

To our best knowledge, our work is the first attempt of directly applying the adjoint-state method for tsunami source inversion. While keeping most of the advantages of the time-reversal imaging, the adjoint approach also recovers the correct tsunami source amplitude. Compared to conventional Greens-function-based inversion (Hossen, Cummins, Dettmer, & Baba, 2015), the adjoint method reproduces the tsunami initial water elevation typically through only a few iterations, which significantly reduces the computational cost.

2 Method

The adjoint-state tsunami source inversion method is designed to resolve the initial water elevation of the tsunami source. The inversion architecture is basically a least-squares problem (Schuster, 2017; Tarantola, 1986; Tromp, Tape, & Liu, 2005) minimizing the error between observation and synthetics due to the variation of the tsunami source. For the forward modelling of the tsunami wave propagation, we use the linear form of the shallow water equation:

$$\begin{aligned}
&\frac{\partial h}{\partial t} + H\left(\frac{\partial u}{\partial x} + \frac{\partial v}{\partial y}\right) = 0, \\
&\frac{\partial u}{\partial t} - fv = -g\frac{\partial h}{\partial x} - bu, \\
&\frac{\partial v}{\partial t} + fu = -g\frac{\partial v}{\partial y} - bv
\end{aligned} \tag{1}$$

where h is the tsunami wave height (the length from the free water surface to the mean sea level), which is the main variable of the tsunami waves. b is the bathymetry (the length from the mean sea level to the seafloor), H is the total height of the water volume (the height from the free water surface to the seafloor), f is the Coriolis force term, g is the gravtional acceleration, and u, v are the depth-averaged velocities at x and y direction, respectively. The shallow water equation is valid under the approximation that the tsunami wavelength is far greater than that of the bathymetry. The original form of the shallow water equation is non-linear (Vallis, 2017). For tsunami modelling, it is common to neglect the viscosity of the sea water, which allows us to neglect the non-linear term and obtain the linear form of the shallow water equation (An et al., 2014). Our numerical test also show that the linear shallow water equation is able to reproduce tsunami waveforms almost identical to those generated by the non-linear shallow water equation (Figure S1). Equation (1) is also based on the approximation that $h << H$. Thus under the linear shallow water equation approximation, the tsunami propagation is very similar to the acoustic wave propagation. The initial condition of the equation (1) is:

$$\begin{aligned}
&h(x, y, t = 0) = m(x, y) \\
&u(x, y, t = 0) = 0, \\
&v(x, y, t = 0) = 0
\end{aligned} \tag{2}$$

where the $m(x, y)$ is the initial water elevation, which is the vertical water displacement excited by the earthquake, volcano eruption, landslide, etc. regarding as the tsunami source. Using the linear shallow water wave equation, the tsunami source can be mapped to synthetic data with a linear propagation operator:

$$d = \mathbf{L}m \tag{3}$$

where $\mathbf{L}$ is the wave propagation matrix, m is the source model of initial water displacement, d is the synthetic tsunami wave field. In tsunami inversion, we compute the linear operator L using the shallow water wave equations. Let m_0 be the starting model of the initial water elevation. Under the Born approximation, the perturbed wavefield δd is linearly related to the source perturbation δm:

$$\delta d = \mathbf{L}\delta m \tag{4}$$

We use the least-square waveform misfit functional to measure how well the synthetics fits the observations. The misfit functional is:

$$J = \frac{1}{2}\|d_{obs} - \mathbf{L}m\|_2^2 \tag{5}$$

where d_{obs} is the observed tsunami waveform. Following the adjoint-state method (Plessix et al., 2006; Tromp et al., 2004), the gradient of the misfit function g at the kth iteration is:

$$g_k = \mathbf{L}^*(d_{obs} - \mathbf{L}m_k) \tag{6}$$

where $d_k = d_{obs} - \mathbf{L}m_k$ is the residue between the observed waveform and model prediction. $\mathbf{L}^*$ is the adjoint operator of the wave propagation operator $\mathbf{L}$. Because the equations (1) are acoustic wave equations, the adjoint wavefield of tsunami waves can be defined similarly to the acoustic adjoint wavefield. Thus the adjoint wavefield $\mathbf{L}^*d_k$ can be calculated by back-propagating the time-reversed data residue at each of the stations to the source region. The gradient of the misfit function g_k is the adjoint wavefield itself (Plessix, 2006; Tarantola, 1986; Tromp et al., 2005). To minimize the misfit function, a conjugate gradient method is used to iteratively update the model. The model perturbations at the kth iteration is calculated by:

$$\delta m_k = \mathbf{C}g_k + \beta\delta m_{k-1} \tag{7}$$

where $\mathbf{C}$ is the pre-conditioning matrix, and β is given by

$$\beta = \frac{g_k^*\mathbf{C}g_k}{g_{k-1}^*\mathbf{C}g_{k-1}} \tag{8}$$

Finally, the model is updated by

$$m_{k+1} = m_k - \alpha\delta m_k \tag{9}$$

Where the step length α is given by

$$\alpha = \frac{(\delta m_k)^* g_k}{(\mathbf{L}\delta m_k)^*(\mathbf{L}\delta m_k)} \tag{10}$$

The sparse and uneven distribution of the tsunami stations may influence the convergence and cause artifacts in the inversion. For example, for the Chilean subduction zone, the tsunami observations are dominated by the IOC coastal gauges along the coast, while DART stations are relatively sparse in the open ocean (Fig. 5). To mitigate the artifacts caused by unevenly distributed tsunami stations, we introduce a weighting function inversely proportional to the azimuth interval between stations. The weighted misfit function J' is given by:

$$J' = \frac{1}{2}\sum_{i=1}^{N} w^{(i)} \| d_{obs}^{(i)} - d_{pred}^{(i)} \|_2^2 \tag{11}$$

where $w^{(i)}$ is the weighting function for the ith station, and $d_{pred}^{(i)}$ is the predicted waveform for the ith station. In exploration seismology, the adjoint-state method is sensitive to the starting velocity model (Schuster, 2017). Similarly, in tsunami source inversion, it is sensitive to bathymetry. The starting model is another important factor for the adjont-state inversion. A well-chosen initial model can speed up the convergence and is less prone to the local minima. We generate the starting model based on the initial water source constrained by the time-reversal imaging method (An & Meng, 2017). Although the source amplitude in time-reversal imaging is less reliable than the source location, it provides a reasonable initial guess, which is critical for the adjoint-state inversion. The workflow of this method is summarized in Fig. 1.

Figure 1. The workflow of the adjoint-state tsunami source inversion method

3 Synthetic Tests

We conduct two numerical synthetic tests to validate this new method for our major concerns: 1) constraining the source mechanisms of tsunamigentic earthquakes without the knowledge of fault geometry and parameters; and 2) improving the tsunami source inversion resolution to detect possible secondary sources, such as co-seismic landslides. The first synthetic test demonstrates the effect of the fault-geometry uncertainty. Since performing a finite-fault slip inversion requires a priori information such as the fault geometry and rigidity. However, many large intraplate earthquakes occur in fault zones of complicated and previously unknown geometry. These unknown fault parameters impose additional uncertainties to the model space of an already ill-posed problem. In comparison, Adjoint-state inversion of tsunami initial water elevation does not rely on the fault geometry, which potentially produces more accurate and realistic result especially for earthquakes without well-defined fault structures. We solve for the initial water elevation and slip distribution of a hypothetical rupture using the fault and receiver setup of the 2014 M8.1 Chile-Iquique tsunami event (Fig. 2). The synthetic tsunami waveforms are recorded at Intergovernmental Oceanographic Commission (IOC) sea level stations along the Chilean coast, and a few DART stations in southeastern Pacific. Two gauge stations and two DART stations are in red for further waveform comparison (Fig. 2). We place a thrust earthquake (strike: 350°, dip: 15°, rake: 90°) centered at the epicenter of the Iquique earthquake, marked with a yellow parallelogram in Fig. 2, and the detailed slip distribution is shown in the inner panel of Fig. 2. We simulate the tsunami wave with the Cornell Multi-grid Coupled Tsunami solver (COMCOT, Liu, Woo, and Cho (1998); Wang and Liu (2006, 2007)). The numeical package COMCOT can perform the forward and the back-propagation simulation using the linear shallow water equation. The tsunami source can be given by either the initial water elevation or the fault slip model. If the tsunami source is given by the fault slip model, the fault slip will be first converted to the seafloor deformation using Okada's equation for the half-space (Okada, 1985), and then the initial water elevation is set as the seafloor deformation. The tsunami waveform is simulated by solving the linear shallow water equation with a staggered-grid finite-difference numerical scheme.

Figure 2. Synthetic model of the comparison of the adjoint-state method and the traditional finite-faule inversion method. Outer panel: study region, bathymetry and stations. Inner panel: input finite-fault slip model. The triangles are the tsunami stations while the red ones D1, D2, G1 and G2 are selected DART and gauge stations for plotting the data misfit.

To mimic the uncertainty of fault geometry, we conduct the finite-fault inversion with slightly different fault parameters (strike: 360°, dip: 20°, rake: 90°). In this synthetic test, the finite-fault inversion is a linear inversion based on Green's functions mapping the unit slip at each finite-fault grids to the stations. We applied the finite-fault source inversion scheme combined with the COMCOT. The recovered slip pattern and corresponding initial water elevation are shown in Fig. 3a and 3c, respectively. Although the fault geometry error is minor (10° in strike and 5° in dip), the reproduced slip pattern is substantially distorted and leads to 20 km eastward shift in the location of the initial seafloor deformation (Fig. 3c). In comparison, the adjoint-state method almost recovers identical amplitude and area of the input initial water elevation (Fig. 4a). Compared to the initial water elevation for our input model (Fig. 4c), the adjoint-state method obtains an initial water elevation method nearly identical to the original input source. The adjoint-state also produces a better waveform fitting than the finite fault model (Fig. 3b and 4b) with the total least-square misfit of the data and the synthetics reduced by approximately 10%.

Figure 3. a) inverted finite-fault slip model with unclear fault geometry; b) predicted (red) and synthetic (blue) waveform for the finite-fault inversion; 3) initial water elevation calculated from the inverted finite-fault slip model

Figure 4. a) initial water elevation obtained by the adjoint-state method; b) predicted (red) and synthetic (blue) waveform for the adjoint-state method; 3) initial water elevation calculated from the input finite-fault slip model (as a reference)

Another synthetic test is designed to demonstrate the ability of resolving possible secondary sources. The landslide often occurs far away from the fault zone and is small in scale. Here we design a synthetic source with a major and a minor regions of binary water elevation variations (Fig. 5, inner panel). For the adjoint-state inversion method, we can mesh the source region with a 2.5 arc-minute ($\approx$ 4.6 km) spacing high resolution grids, which contains 30 * 80 grid points. The adjoint-state inversion result is plotted in Fig. 6, with the sample data fitting figures for two gauge stations and one DART station marked in red shown in Fig. 5. The adjoint-state image is obtained after 20 iterations. As a comparison, the conventional Greens-function-based inversion that has similar computation time can only take 6 * 16 grids with spacing of 10 arc-minute ($\approx$ 18.4 km). The sparse grid may not resolve the secondary sources (Fig. S5).

We observe that in the adjoint-state solution, both the major and the secondary sources are properly recovered. The data fitting is nearly perfect shown in Fig. 6a, and

Figure 5. Synthetic model of the demonstration of resolving secondary tsunami sources. Outer panel: study region, bathymetry and stations. It is also the study region of the 2014 Chile-Iquique tsunami event. Inner panel: the input initial water elevation model. Triangles with station names (except G1) are the tsunami stations used in the Chile-Iquique tsunami inversion. All stations are used in the synthetic test.

Figure 6. a): predicted (red) and synthetic (blue) waveform for the adjoint-state inversion in the selected 3 stations; b): initial water elevation obtained by adjoint-state inversion; c): the convergence plot. The source grid spacing is 2.5 arc-minute (4.6 km).

the data misfit shows fast decrease in the first 5 iterations, and finally the misfit is reduced by 99%. Under the same computational cost restriction, the linear inversion with Green's functions may also fit the data well (Fig. S5), but the misfit of the coda wave and some high frequency part observed in station G2 and D1 is large, which suggests that the secondary sources only produce minor waveform variations. The overall misfit reduction between the adjoint-state method with 30*80 grids and the linear inversion with 6*16 grids is about 30%. The secondary source may also be resolved by the linear waveform inversion method with the same 30 * 80 grids mesh, which requires to calculate the Greens function with shallow-water wave simulation 2,400 times, a huge computational cost compared to the adjoint-state method. Theoretically, the adjoint-state method only needs to compute the tsunami wave simulation twice the number of iterations. In our test example, one simulation takes about 7 minutes, and the adjoint-state method takes about 4.7 hours for 20 iterations. In the synthetic test of the Green's-function-based method, it takes 11.2 hours for only 6*16 grids, and will take 280 hours to reach the same resolution with 30*80 grids. With the high computation efficiency, we expect the adjoint-state inversion method to be effective in obtaining high-resolution tsunami source image, which is crucial for identifying possible seafloor activities associated with coseismic landslides and other secondary sources.

Since the tsunami waves have long wavelength (about 100km), the half-wavelength resolution limit is around 50 km. But the full waveform information may help to resolve the initial water elevation pattern smaller than half wavelength. More synthetic tests are conducted to demonstrate the potential sub-wavelength resolution of the proposed adjoint-state method. The test with a 30*30 km secondary source (Figure S2a, the main source, bathymetry and stations are the same as the secondary source test of Figure 5). The main pattern of the secondary source can still be clearly recognized, but it is dimmed and the amplitude cannot be fully recovered. A 20*20 km secondary source (Figure S2b) cannot be clearly imaged. For a very small sub-wavelength secondary tsunami source, the invertion result restores the location and basic pattern, but the recovered amplitude is significantly smaller, and the area of inverted source is getting larger than the input model. We interpret this feature as the smearing effect due to limited spatial resolution.

The inaccuracy of bathymetry data induce artifacts and convergence issue to the adjoint-state inversion. According to our numerical test, if the bathymetry model is accurate, the inversion is quite stable with fast convergence rate. In such cases the starting model has less impact on the inversion result (Figure S3 a-d). We imposed 10% bathymetry perturbation that follows Von Karman distribution with 100 km correlation length. In that case, the inversion becomes less stable and the convergence rate slows down. The inversion results are containmated with artifacts due to the incorrect Green's function (Figure S3 e-h).

4 Application to the 2014 Chile-Iquique Tsunami Event

To understand the performance of the adjoint-state method on real tsunami events, we inverted the initial water elevation of the 2014 Mw 8.1 Chile-Iquique tsunami event, and compare our results with the conventional methods including time-reversal imaging and finite fault inversions. We adopt the recordings of 4 DART stations and 17 IOC gauge stations (triangles labeled with station names in purple and black, respectively, in Fig. 5). The source region is marked with a yellow rectangle, with the red star marking the epicenter of the earthquake. The calculation domain for the tsunami simulation is between 95°W - 70°W and latitude 35°S - 5°S using 3000 * 3600 grids with an interval of 30 arc-seconds. The source region is represented with a rectangle between 71.5°W - 70.3°W and 21°S - 18.5°S, meshed uniformly with 144 * 360 grid points of 30 arc-seconds spacing. The tsunami data are pre-processed such as removing the long-period tidal waves by a polynomial fitting technique, following (An et al., 2014). Then the first peak of the tsunami waveform is manually picked for setting up the time window to fit in the adjoint-state inversion.

Figure 7. Tsunami source inversion result for the 2014 Chile-Iquique event. Central panel: adjoint-state inversion result after 20 iterations; Left panel: predicted (red) and observed (blue) tsunami waveform data for 4 DART stations; Right panel: predicted (red) and observed (blue) tsunami waveform data for 4 IOC gauge stations. The black dashed line separate the first wiggle we used for inversion, and the coda waves.

We use the time-reversal image as our starting model followed by 20 iterations of adjoint-state inversions. We focus on fitting the first wiggle of the tsunami waveforms, because the following coda waves are dominated by multiple reflections along the coast, which introduces artifacts and destabilizes the model convergence since we lack the accurate bathymetry in coastal regions. The predictions generally match the observations well (Fig. 7), although there are minor time shifts in some of the IOC gauge stations. An et al. (2014) observed similar timing issues and concluded that bathymetry errors near the coast are responsible for the mismatch.

In real tsunami event inversion, the inversion is more sensitive to the starting model due to the inaccuracy of bathymetry, the nonlinearity of the inversion problem, and the sparsity and irregularly distributed gauge and/or DART stations. We tested different starting models of zero initial water elevation, the USGS finite-fault model predicted initial water elevation (https://earthquake.usgs.gov/ earthquakes/eventpage/usc000nzvd/finite-fault), and the amplitude-corrected time reversal imaging result (Figure S4a, c and e; corresponding inversion results: Figure S4b, d and f). All inversions have 20 iterations and perform gradient-smoothing. Although the inversion results inhert features of the starting models to some extent, the large-scale pattern of the inversion results are similar. The inversion with the TRI starting model has the minimum data misfit and the largest misfit reduction. Therefore we choose the amplitude-corrected time reversal image as the starting model.

The final inversion of the initial tsunami source is shown in the central panel of Fig. 7. It features positive water elevation to the southeast of the epicenter, and a southwestward extension. Some minor negative water elevation is seen around the coast, which is most likely artifacts related to the coastal reflections. Overall, we considered the preliminary result of the adjoint-state method provides a clear and high-resolution image. We notice that although we intend to fit only the first wiggle, the following coda waves

Figure 8. Comparisons of initial water elevation results obtained by different methods. a)-d): finite-fault inversion by different groups; e) adjoint-state method; f) time-reversal method

are also reasonably matched. Compared with time-reversal imaging (Fig. 8f), our method naturally obtains true amplitude without any additional calibrations. The remaining amplitude mismatch is again likely attributed to the errors of coastal bathymetry. The waveform fitting can be potentially further improved by an empirical calibration method using a large aftershock. In Fig. 8, we compare the tsunami source obtained by the adjoint-state method with those predicted by finite-fault models (An et al., 2014; Gusman et al., 2015; Hayes et al., 2014; Yagi et al., 2014) and by time reversal imaging (An & Meng, 2017). Our preferred result shows similar position of the peak water elevation to Hayes et al. (2014). The southwestward extension resembles to that of Yagi et al. (2014). Overall, the adjoint-state method results in similar image to that of the time-reversal image, with significantly less along-coast reflection artifacts (Fig. 8e and 8f). To conclude, the Iquique example demonstrates that compared with traditional methods, the new adjoint-state approach resolves more detailed source features with stable and fast convergence rate. Our method is also more efficient, less ad-hoc and has less along-coast artifacts.

5 Discussion

5.1 Limitations and further improvements of the adjoint-state tsunami inversion method

In the synthetic test settings, the adjoint-state method has fast convergence rate, enhanced efficiency of resolving small-scale tsunami sources and recovering true source amplitudes. The synthetic tests are not sensitive to the starting model, assuming the satisfication of approximations of the linear shallow water equation and the accuracy of the bathymetry data. Randomized noise seems not influence the convergence too much. In the test case the convergence is not perturbed when 5% noise is added. Also, regardless of the starting model, the inversion converges to the global minimum which is nearly identical to the ground truth. However, the inversion for real tsunami data becomes complicated. First, to apply a straightforward adjoint-state method requires a linear wave equation. The linear shallow water equation is good for small tsunami waves whose amplitude is far smaller than the bathymetry. This approximation is satisfied in the open oceans but may be invalid in the near-coast region where the bathymetry becomes shallow. In our numerical test (Figure S1), the difference between the results of linear and nonlinear shallow water equations are small, even for the near-coast gauge stations especially for the first wiggle of the waveform. So it would be safe to apply the linear shallow water equation. This feature is also reported by An et al. (2014).

Second, the bathymetry and the coastline data do not have enough accuracy. Currently, we use the 30-arc-second bathymetry, which may not be accurate enough to perform the source inversion. The inaccurate bathymetry introduces error to the wave propagation and the adjoint wavefield, which renders the adjoint wavefield no longer the gradient of the misfit functional. In this case, the convergence is less stable, resulting in a slow convergence rate and artifacts in the inversion results. The inversion also becomes depending on the starting model. Inaccurate coastline produces additional non-existing reflections contaminating the coda wave. Applying a higher resolution bathymetry data especially in the shallow along-coast region is critical to simulate reflections and provide a possibility to fit the coda waves. Kubota et al. (2018) reported that a 4 arc-second bathymetry could model the coastal reflection, which may be good for the adjoint inversion but more tests are needed. This issue may also be mitigated by only accounting the first wiggle of the tsunami wave in the inversion, and to apply a proper pre-conditioning method (Chen, Huang, Yao, Hilst, & Niu, 2014; Luo, Modrak, & Tromp, 2013), such as the gradient smoothing (Figure S3 and S4 for more information). Another strategy to mitigate the inaccuracy of the propagation matrix is to account for the Green's function uncertainty in the misfit functional (Yagi & Fukahata, 2011). This particular approach can be potentially incorporated into our inversion scheme if the gradient of the modified misfit functional can be derived from the adjoint wave-field. Applying a different misfit functional may be another solution. In earthquake seismology, various misfit functional has been explored, including the waveform similarity, cross-correlation, and envelop measuring (Bozdağ, Trampert, & Tromp, 2011). In our adjoint-state tsunami inversion, we need to obtain the actual wave height and arrival time for the possible usage of the tsunami warning. Thus we still adopt the standard least-square misfit functional which accounts for both the amplitude and phase information. In our future work, we will explore better misfit functionals with measurements that more sensitive to the tsunami source variations.

The sparsely and irregularly distributed gauge and DART stations also pose challenges to the adjoint inversion. The gauge stations are along the coastline, while the DART stations are distributed very sparsely in the open ocean, so the inversion is inevitably biased. Thus, we need a proper station weighting function to mitigate this problem. In this work, an azimuth-based station weighting technique is applied to both the synthetic tests and the real data. But in some cases, certain isolated stations contribute too much to the image. A potential accurate station weighting technique is the adjoint sensitivity weighting method given by Hossen et al. (2018). The idea is to first compute the station sensitivity kernels using the back-propagated data residue of each station, and then weight each station based on the station sensitivity kernels. If the imaging result is highly sensitive to a certain station, then this station should be downweighted. This weighting procedure can be combined with the adjoint inversion. The signal to noise ratio of stations may also need to be considered. Downweighting the noisy stations may reduce the artifacts due to noise. In addition, appropriate good pre-conditioning technique, such as the gradient smoothing, can also accelerate the convergence rate (Hou & Symes, 2017), which enhances the real-time applicability of the adjoint-state method for tsunami warning and hazard mitigation.

Despite these problems, the adjoint-state tsunami inversion method provides more efficient high-resolution tsunami source image without being affected by the unknown fault geometry. In future development, in addition to obtaining more accurate bathymetry models, the dependence of starting models could be reduced by a more suitable station weighting method, a better misfit functional or applying the multi-scale technique which first fits the low-frequency components of the tsunami waves, and then progresses to fit the higher frequencies. In the current stage, we compare the data misfit of multiple starting models to determine the optimal initial model. In the case of the Iquique earthquake, the time-reversal imaging model leads to the smallest data misfit and is our preferred initial model (Fig. S4).

5.2 Efficient tsunami warning with faster and more accurate wave height prediction

The key to tsunami warning is speed and accuracy. Currently, the common practice for tsunami warning is to constrain the earthquake moment and centroid location using teleseismic W phases (Kanamori & Rivera, 2008) and estimate the tsunami arrival time and wave height using previously calculated tsunami scenarios. Real-time finite-fault modeling based on landward GPS and strong-motion stations generate more detailed earthquake source information (Bock, Melgar, & Crowell, 2011), but still lack the constraint of the shallow near-trench slip that contributes most to the tsunami generation. Moreover, shallow secondary tsunami sources of coseismic landslide or triggering on splay faults enlarge the tsunami height but are often missed by the finite-fault inversions. To consider all tsunamigenic sources and predict accurate wave heights, initial water elevation inversion is important. In light of the recent development of global DART and coastal tide gauge network, particularly in the Pacific and Indian Ocean, its promising to explore real-time initial water elevation inversion for tsunami early warning purpose in major subduction zones (e.g. Alaska, Japan, Chile and Sumatra) Hossen, Cummins, Roberts, and Allgeyer (2015). Among available tsunami source imaging techniques, the time-reversal imaging method does not recover true amplitudes. The Greens-function-based inversion methods suffer from heavy computational burden and is limited to pre-calculated tsunami scenarios. For example, if we mesh the entire south American subduction zones with a 1 arc-minute spacing, the total number of grids will be about 800,000, which requires several months or even years to calculate the Greens functions with hundreds of CPU cores, and takes more than 100 TB storage space. On the other hand, the adjoint-state tsunami inversion is suitable for real-time application because it recovers accurate initial water elevation in only a few iterations. The tsunami source image can be then quickly and directly used in forward tsunami simulations, producing accurate forecast of tsunami height and arrival time. We expect that the adjoint-state will be particularly useful to improve the far-field or transoceanic tsunami predictions since the near-field DART and coastal tide gauge can be used as the input.

6 Conclusion

Currently, we have developed the initial theoretical and numerical framework for the adjoint-state method for tsunami initial water elevation inversion. We validate the ability of our approach to resolve the primary and secondary tsunami sources through synthetic tests. The preliminary work above describes the basis of the adjoint-state full waveform tsunami source inversion, validates the effectiveness and feasibility of the method, and reveals some aspects for further developing this method. With this adjoint-state tsunami source inversion method, we are able to better resolve small-scale tsunami sources with high resolution and less computational time, especially for some fault zones without detailed structures. This method may also contribute to the tsunami warning systems.

Acknowledgments

This work is supported by NSF funding 1833532, by the Leon and Joanne V.C. Knopoff Fund, and by the Peking Unversity Exchange Research Grant for Ph.D students. We thank the General Bathymetric Chart of the Oceans (www.gebco.net) for providing high resolution bathymetry data, Sea Level Station Monitoring Facility, Intergovernmental Oceanographic Commission of UNESCO (www.ioc-sealevelmonitoring.org) for providing the tide gauge data, and NOAA Center for Tsunami Research (https://nctr.pmel.noaa.gov/Dart/) for providing DART data. We appreciate the authors of the COMCOT software package (http://223.4.213.26/archive/tsunami/ cornell/comcot_down.htm). We also thank Chao An for his valuable discussions in developing the adjoint method and writing the manuscript. The final tsunami source model of the 2014 Chile-Iquique tsunami event is open for download at https://zenodo.org/record/2833419.

References

Adriano, B., Fujii, Y., Koshimura, S., Mas, E., Ruiz-Angulo, A., & Estrada, M. (2018). Tsunami source inversion using tide gauge and dart tsunami waveforms of the 2017 mw8. 2 mexico earthquake. *Pure and Applied Geophysics*, *175*(1), 35–48.

An, C., & Meng, L. (2017). Time reversal imaging of the 2015 illapel tsunami source. *Geophysical Research Letters*, *44*(4), 1732–1739.

An, C., Sepúlveda, I., & Liu, P. L.-F. (2014). Tsunami source and its validation of the 2014 iquique, chile, earthquake. *Geophysical Research Letters*, *41*(11), 3988–3994.

Bock, Y., Melgar, D., & Crowell, B. W. (2011). Real-time strong-motion broadband displacements from collocated gps and accelerometers. *Bulletin of the Seismological Society of America*, *101*(6), 2904–2925.

Bozdağ, E., Trampert, J., & Tromp, J. (2011). Misfit functions for full waveform inversion based on instantaneous phase and envelope measurements. *Geophysical Journal International*, *185*(2), 845–870.

Chen, M., Huang, H., Yao, H., Hilst, R., & Niu, F. (2014). Low wave speed zones in the crust beneath se tibet revealed by ambient noise adjoint tomography. *Geophysical Research Letters*, *41*(2), 334–340.

Feng, Z., & Schuster, G. T. (2017). Elastic least-squares reverse time migration.

Geophysics, *82*(2), S143–S157.

Fujii, Y., Satake, K., Sakai, S., Shinohara, M., & Kanazawa, T. (2011). Tsunami source of the 2011 off the pacific coast of tohoku earthquake. *Earth, planets and space*, *63*(7), 55.

Grilli, S. T., Harris, J. C., Bakhsh, T. S. T., Masterlark, T. L., Kyriakopoulos, C., Kirby, J. T., & Shi, F. (2013). Numerical simulation of the 2011 tohoku tsunami based on a new transient fem co-seismic source: Comparison to far-and near-field observations. *Pure and Applied Geophysics*, *170*(6-8), 1333–1359.

Gusman, A. R., Murotani, S., Satake, K., Heidarzadeh, M., Gunawan, E., Watada, S., & Schurr, B. (2015). Fault slip distribution of the 2014 iquique, chile, earthquake estimated from ocean-wide tsunami waveforms and gps data. *Geophysical Research Letters*, *42*(4), 1053–1060.

Hayes, G. P., Herman, M. W., Barnhart, W. D., Furlong, K. P., Riquelme, S., Benz, H. M., ... Samsonov, S. (2014). Continuing megathrust earthquake potential in chile after the 2014 iquique earthquake. *Nature*, *512*(7514), 295.

Heidarzadeh, M., Harada, T., Satake, K., Ishibe, T., & Gusman, A. R. (2016). Comparative study of two tsunamigenic earthquakes in the solomon islands: 2015 mw 7.0 normal-fault and 2013 santa cruz mw 8.0 megathrust earthquakes. *Geophysical Research Letters*, *43*(9), 4340–4349.

Hoshiba, M., & Ozaki, T. (2014). Earthquake early warning and tsunami warning of the japan meteorological agency, and their performance in the 2011 off the pacific coast of tohoku earthquake mw 9.0. In *Early warning for geological disasters* (pp. 1–28). Springer.

Hossen, M. J., Cummins, P. R., Dettmer, J., & Baba, T. (2015). Time reverse imaging for far-field tsunami forecasting: 2011 tohoku earthquake case study. *Geophysical Research Letters*, *42*(22), 9906–9915.

Hossen, M. J., Cummins, P. R., Roberts, S. G., & Allgeyer, S. (2015). Time reversal imaging of the tsunami source. *Pure and Applied Geophysics*, *172*(3-4), 969–984.

Hossen, M. J., Gusman, A., Satake, K., & Cummins, P. R. (2018). An adjoint sensitivity method applied to time reverse imaging of tsunami source for the 2009 samoa earthquake. *Geophysical Research Letters*, *45*(2), 627–636.

Hou, J., & Symes, W. (2017). True amplitude imaging for incomplete seismic data. In *Seg technical program expanded abstracts 2017* (pp. 4534–4539). Society of Exploration Geophysicists.

Kanamori, H., & Rivera, L. (2008). Source inversion ofwphase: speeding up seismic tsunami warning. *Geophysical Journal International*, *175*(1), 222–238.

Kubota, T., Saito, T., Ito, Y., Kaneko, Y., Wallace, L. M., Suzuki, S., ... Henrys, S. (2018). Using tsunami waves reflected at the coast to improve offshore earthquake source parameters: Application to the 2016 mw 7.1 te araroa earthquake, new zealand. *Journal of Geophysical Research: Solid Earth*, *123*(10), 8767–8779.

Larmat, C., Montagner, J.-P., Fink, M., Capdeville, Y., Tourin, A., & Clévédé, E. (2006). Time-reversal imaging of seismic sources and application to the great sumatra earthquake. *Geophysical Research Letters*, *33*(19).

Lay, T., Yue, H., Brodsky, E. E., & An, C. (2014). The 1 april 2014 iquique, chile, mw 8.1 earthquake rupture sequence. *Geophysical Research Letters*, *41*(11), 3818–3825.

Liu, P. L., Woo, S.-B., & Cho, Y.-S. (1998). Computer programs for tsunami propagation and inundation. *Cornell University*, *25*.

Luo, Y., Modrak, R., & Tromp, J. (2013). Strategies in adjoint tomography. *Handbook of Geomathematics*, 1–52.

MacInnes, B. T., Gusman, A. R., LeVeque, R. J., & Tanioka, Y. (2013). Comparison of earthquake source models for the 2011 tohoku event using tsunami simulations and near-field observations. *Bulletin of the Seismological Society of America*, *103*(2B), 1256–1274.

Maeda, T., Furumura, T., Sakai, S., & Shinohara, M. (2011). Significant tsunami observed at ocean-bottom pressure gauges during the 2011 off the pacific coast of tohoku earthquake. *Earth, Planets and Space*, *63*(7), 53.

Moore, A. M. (1991). Data assimilation in a quasi-geostrophic open-ocean model of the gulf stream region using the adjoint method. *Journal of Physical Oceanography*, *21*(3), 398–427.

Mulia, I. E., Gusman, A. R., Jakir Hossen, M., & Satake, K. (2018). Adaptive tsunami source inversion using optimizations and the reciprocity principle. *Journal of Geophysical Research: Solid Earth*, *123*(12), 10–749.

Nakata, N., & Beroza, G. C. (2016). Reverse time migration for microseismic sources using the geometric mean as an imaging condition. *Geophysics*, *81*(2), KS51–KS60.

Okada, Y. (1985). Surface deformation due to shear and tensile faults in a half-space. *Bulletin of the seismological society of America*, *75*(4), 1135–1154.

Plessix, R.-E. (2006). A review of the adjoint-state method for computing the gradient of a functional with geophysical applications. *Geophysical Journal International*, *167*(2), 495–503.

Satake, K. (2014). Advances in earthquake and tsunami sciences and disaster risk reduction since the 2004 indian ocean tsunami. *Geoscience Letters*, *1*(1), 15.

Satake, K., Fujii, Y., Harada, T., & Namegaya, Y. (2013). Time and space distribution of coseismic slip of the 2011 tohoku earthquake as inferred from tsunami waveform data. *Bulletin of the seismological society of America*, *103*(2B), 1473–1492.

Schuster, G. T. (2017). *Seismic inversion.* Society of Exploration Geophysicists.

Somala, S. N., Ampuero, J.-P., & Lapusta, N. (2018). Finite-fault source inversion using adjoint methods in 3-d heterogeneous media. *Geophysical Journal International*, *214*(1), 402–420.

Sun, J., Xue, Z., Zhu, T., Fomel, S., & Nakata, N. (2016). Full-waveform inversion of passive seismic data for sources and velocities. In *Seg technical program expanded abstracts 2016* (pp. 1405–1410). Society of Exploration Geophysicists.

Tappin, D. R., Grilli, S. T., Harris, J. C., Geller, R. J., Masterlark, T., Kirby, J. T., ... Mai, P. M. (2014). Did a submarine landslide contribute to the 2011 tohoku tsunami? *Marine Geology*, *357*, 344–361.

Tarantola, A. (1986). A strategy for nonlinear elastic inversion of seismic reflection data. *Geophysics*, *51*(10), 1893–1903.

Tromp, J., Tape, C., & Liu, Q. (2005). Seismic tomography, adjoint methods, time reversal and banana-doughnut kernels. *Geophysical Journal International*, *160*(1), 195–216.

Vallis, G. K. (2017). *Atmospheric and oceanic fluid dynamics.* Cambridge University Press.

Virieux, J., & Operto, S. (2009). An overview of full-waveform inversion in exploration geophysics. *Geophysics*, *74*(6), WCC1–WCC26.

Wang, X., & Liu, P. L.-F. (2006). An analysis of 2004 sumatra earthquake fault plane mechanisms and indian ocean tsunami. *Journal of Hydraulic Research*, *44*(2), 147–154.

Wang, X., & Liu, P. L.-F. (2007). Numerical simulations of the 2004 indian ocean tsunamiscoastal effects. *Journal of Earthquake and Tsunami*, *1*(03), 273–297.

Wei, Y., Chamberlin, C., Titov, V. V., Tang, L., & Bernard, E. N. (2013). Modeling of the 2011 japan tsunami: Lessons for near-field forecast. *Pure and Applied Geophysics*, *170*(6-8), 1309–1331.

Yagi, Y., & Fukahata, Y. (2011). Introduction of uncertainty of green's function into waveform inversion for seismic source processes. *Geophysical Journal International*, *186*(2), 711-720.

Yagi, Y., Okuwaki, R., Enescu, B., Hirano, S., Yamagami, Y., Endo, S., & Komoro, T. (2014). Rupture process of the 2014 iquique chile earthquake in relation with the foreshock activity. *Geophysical Research Letters*, *41*(12), 4201–4206.

Yue, H., Lay, T., Rivera, L., An, C., Vigny, C., Tong, X., & Soto, J. C. B. (2014). Localized fault slip to the trench in the 2010 maule, chile mw= 8.8 earthquake from joint inversion of high-rate gps, teleseismic body waves, insar, campaign gps, and tsunami observations. *Journal of Geophysical Research: Solid Earth*, *119*(10), 7786–7804.

Figure 1.

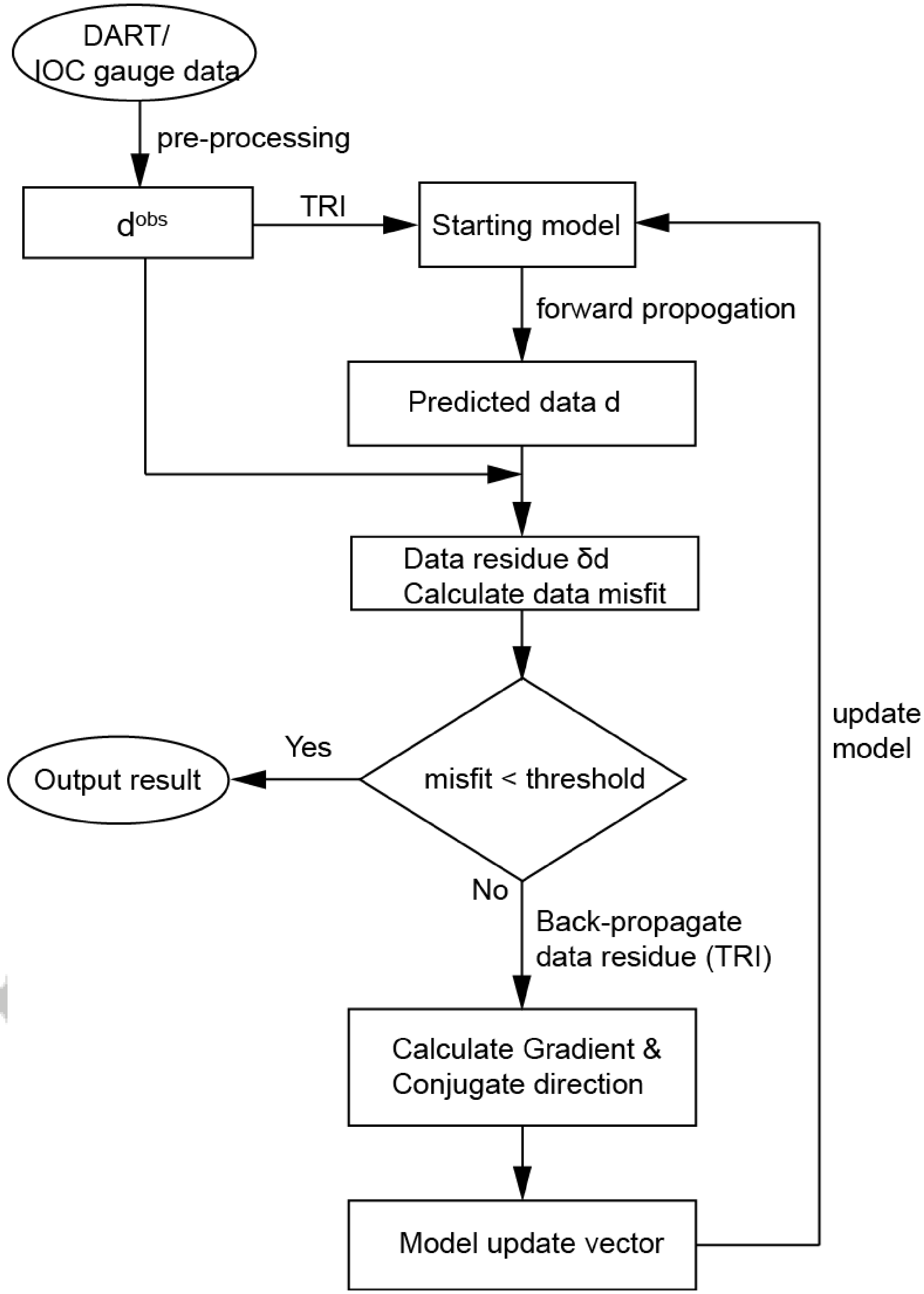
DART/
IOC gauge data
pre-processing
d^obs
TRI
Starting model
forward propogation
Predicted data d
Data residue δd
Calculate data misfit
Yes
Output result
misfit < threshold
No
Back-propagate
data residue (TRI)
Calculate Gradient &
Conjugate direction
Model update vector
update
model

Figure 2.

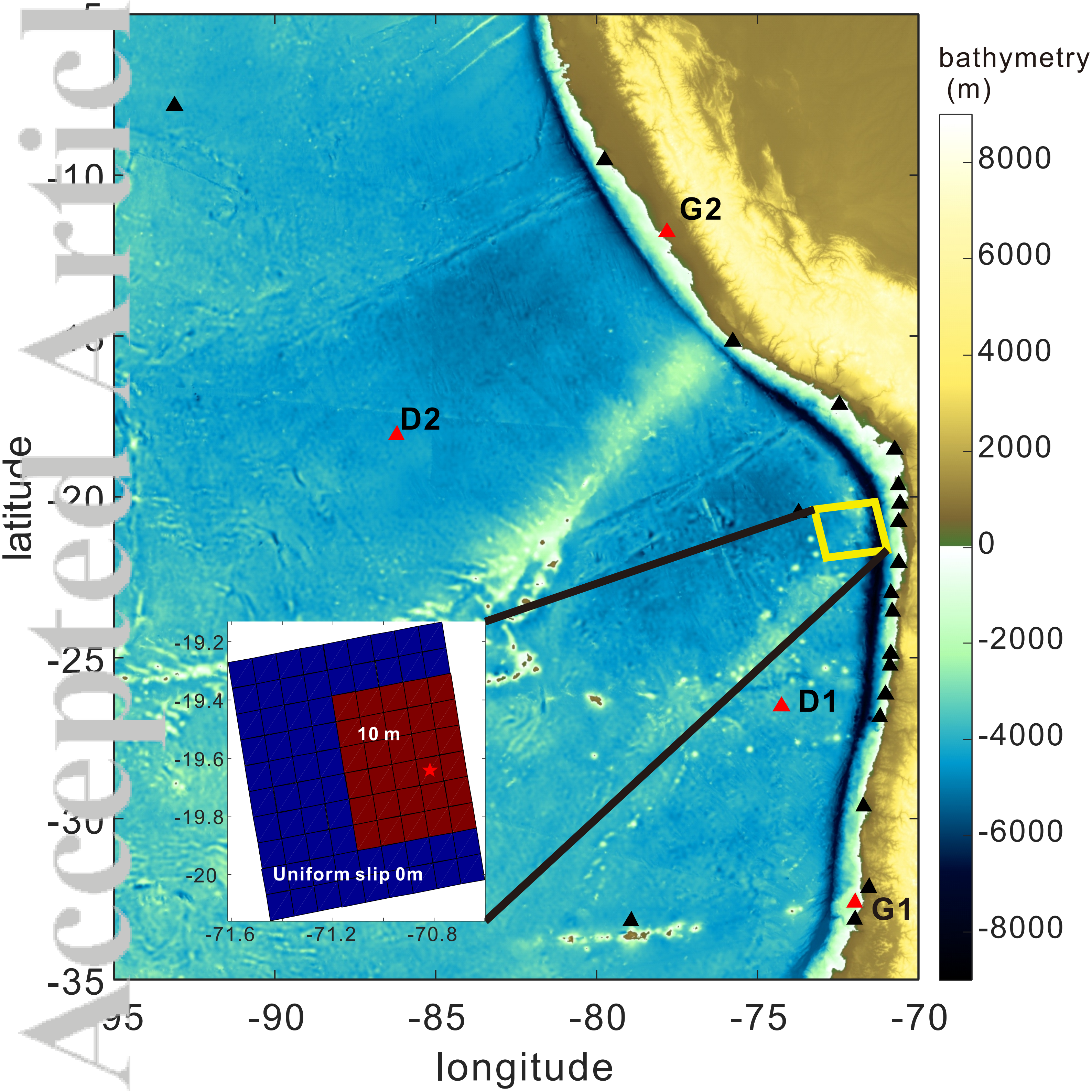
bathymetry (m)
8000
6000
4000
2000
0
-2000
-4000
-6000
-8000
latitude
-10
-20
-25
-30
-35
longitude
-90
-85
-80
-75
-70
G2
D2
D1
G1
-19.2
-19.4
-19.6
-19.8
-20
-71.6
-71.2
-70.8
10 m
Uniform slip 0m

Figure 3.

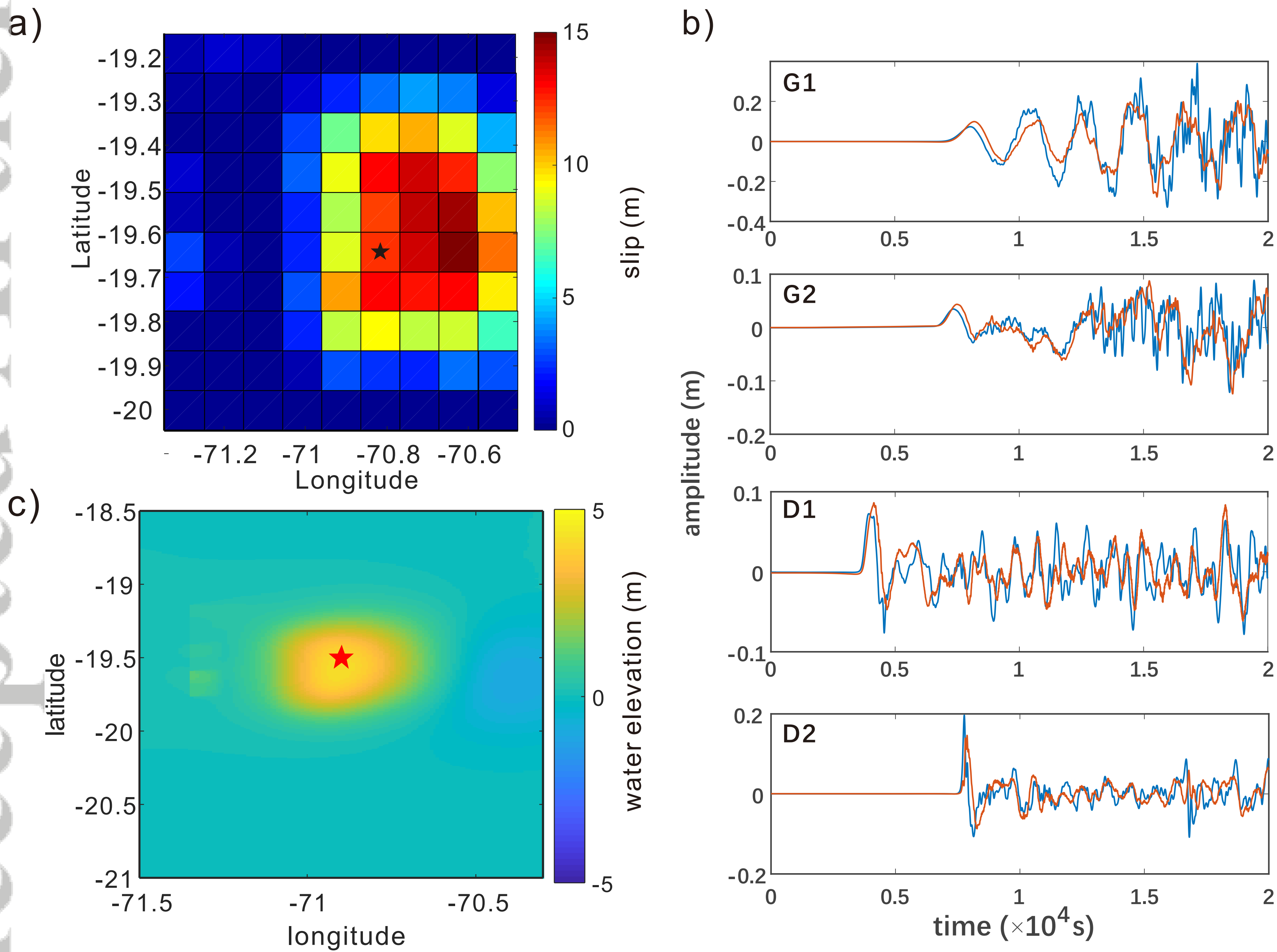
a)
-19.2
-19.3
-19.4
-19.5
-19.6
-19.7
-19.8
-19.9
-20
Latitude
-71.2
-71
-70.8
-70.6
Longitude
15
10
5
0
slip (m)
b)
G1
G2
D1
D2
amplitude (m)
time (×10^4 s)
c)
-18.5
-19
-19.5
-20
-20.5
-21
latitude
-71.5
-71
-70.5
longitude
water elevation (m)

Figure 4.

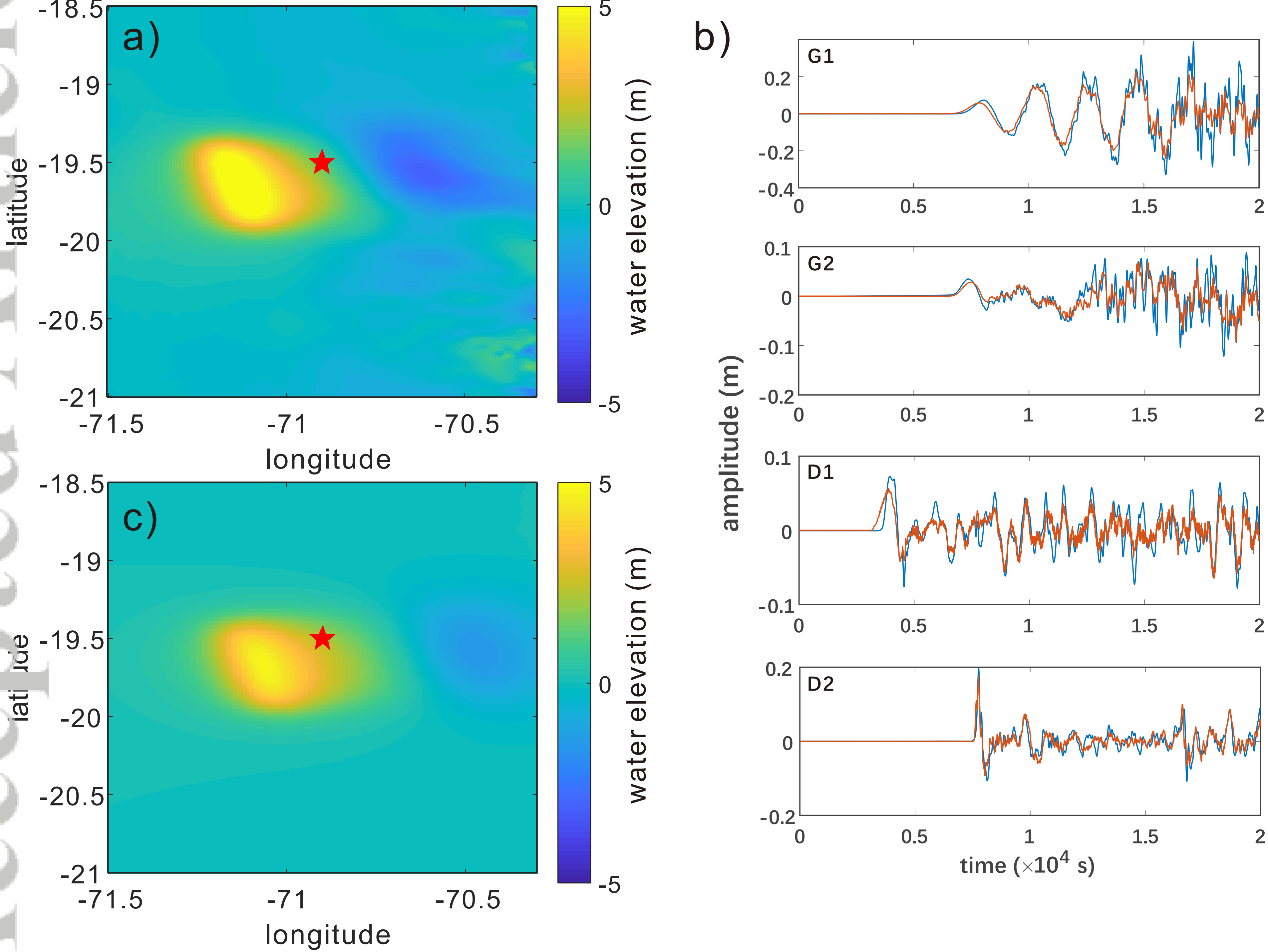

a)
b)
c)
latitude
longitude
water elevation (m)
-18.5
-19
-19.5
-20
-20.5
-21
-71.5
-71
-70.5
5
0
-5
G1
G2
D1
D2
amplitude (m)
time (×10^4 s)
0
0.5
1
1.5
2

Figure 5.

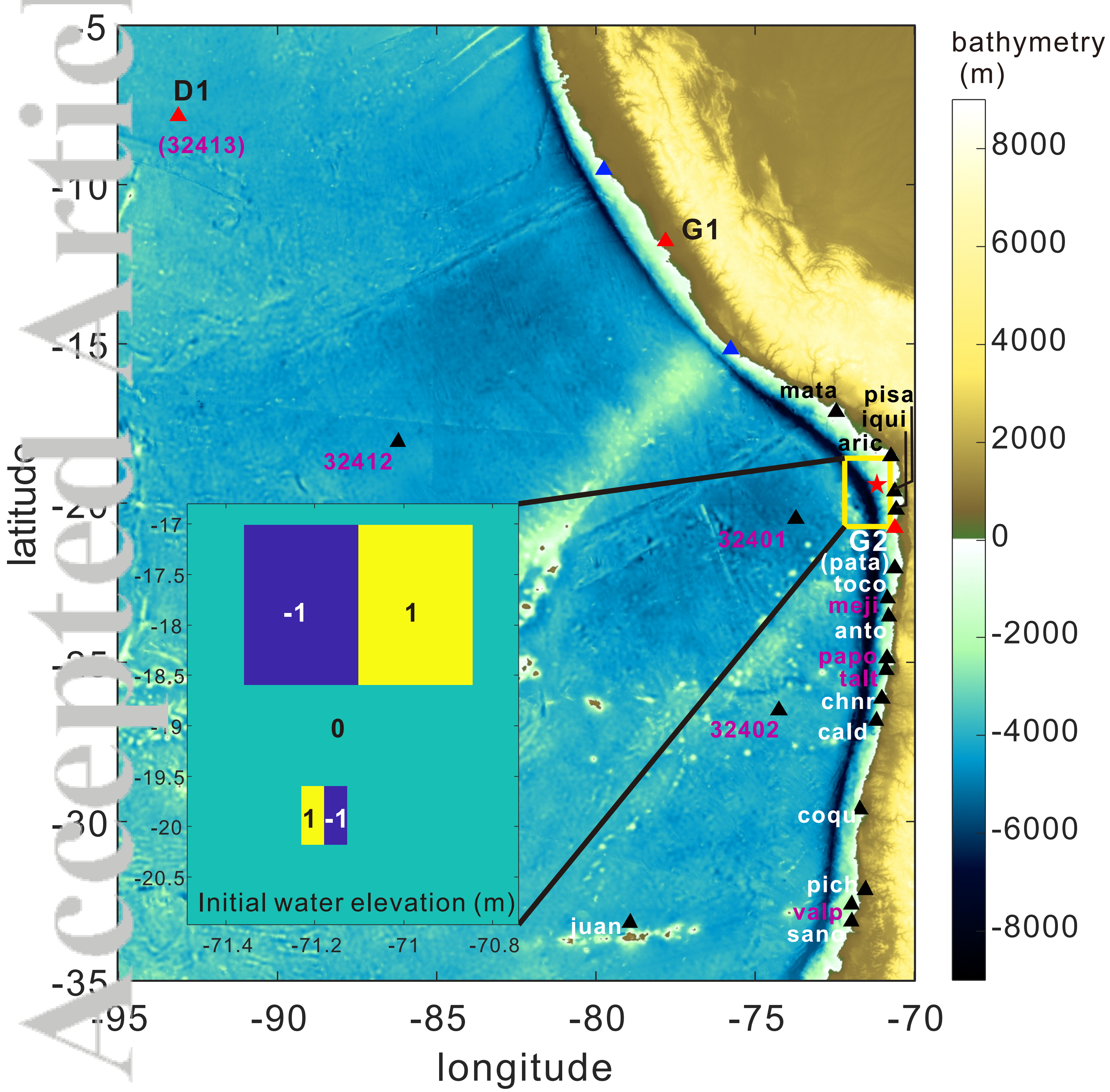

D1
(32413)
G1
32412
mata
pisa
iqui
aric
32401
G2
(pata)
toco
meji
anto
papo
talt
chnr
cald
32402
coqu
pich
valp
sano
juan
Initial water elevation (m)
-1
1
0
1
-1
latitude
longitude
bathymetry (m)

Figure 6.

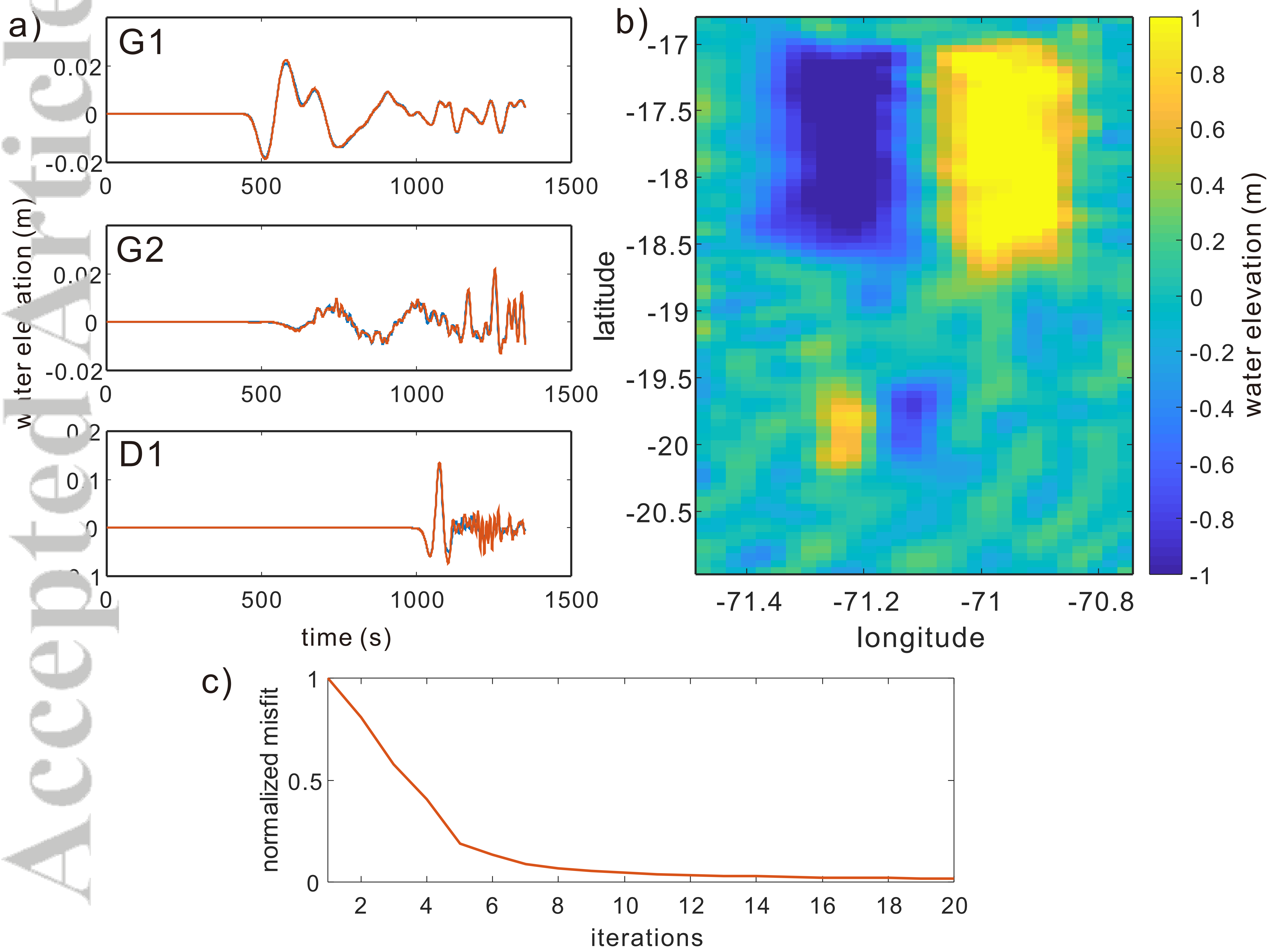
a)
G1
G2
D1
0.02
0
-0.02
0.2
0.1
-0.1
0
500
1000
1500
water elevation (m)
time (s)
b)
-17
-17.5
-18
-18.5
-19
-19.5
-20
-20.5
latitude
-71.4
-71.2
-71
-70.8
longitude
1
0.8
0.6
0.4
0.2
0
-0.2
-0.4
-0.6
-0.8
-1
water elevation (m)
c)
1
0.5
0
normalized misfit
2
4
6
8
10
12
14
16
18
20
iterations

Figure 7.

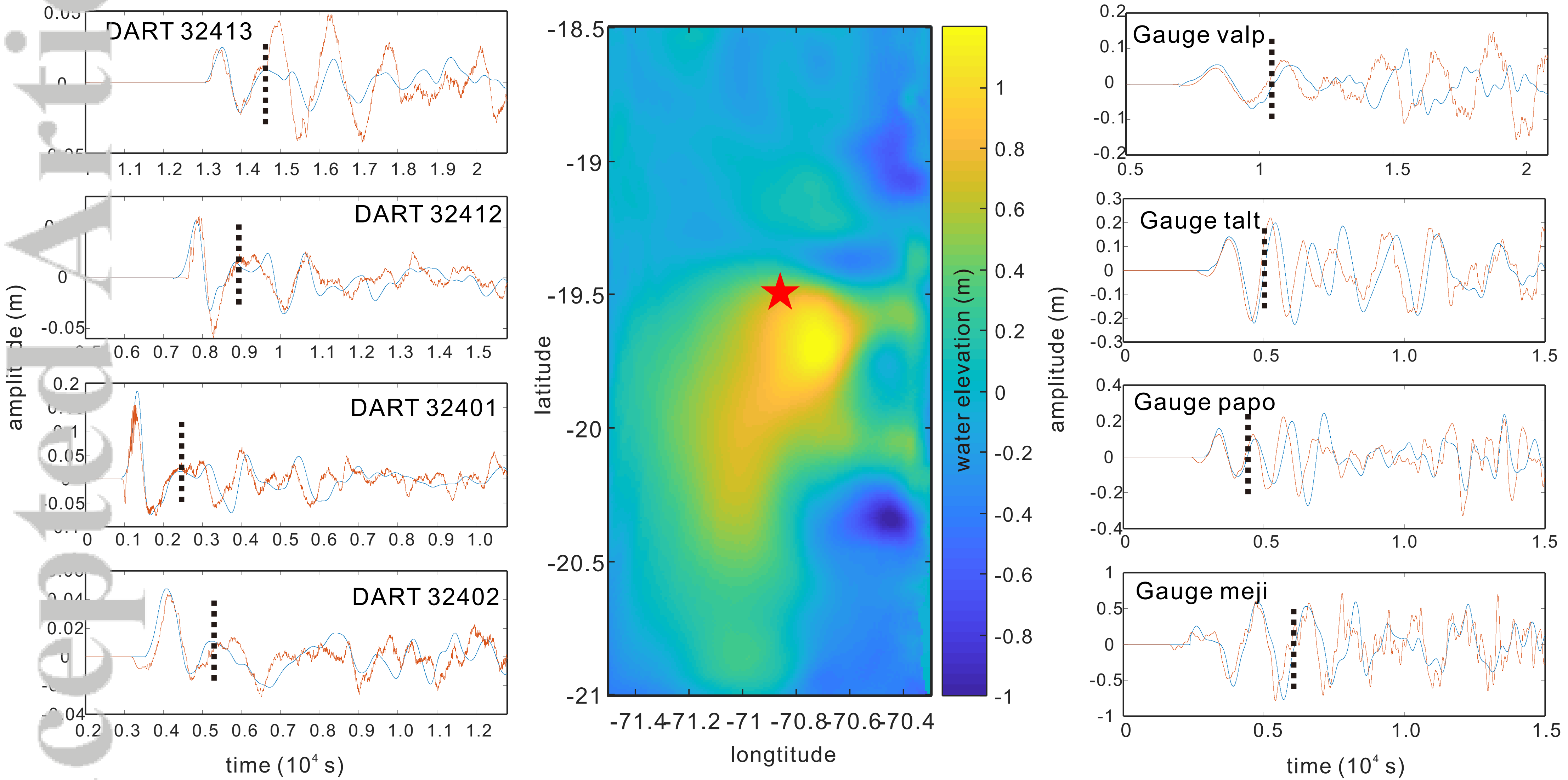
DART 32413
DART 32412
DART 32401
DART 32402
amplitude (m)
time (10⁴ s)
latitude
longtitude
water elevation (m)
Gauge valp
Gauge talt
Gauge papo
Gauge meji

Figure 8.

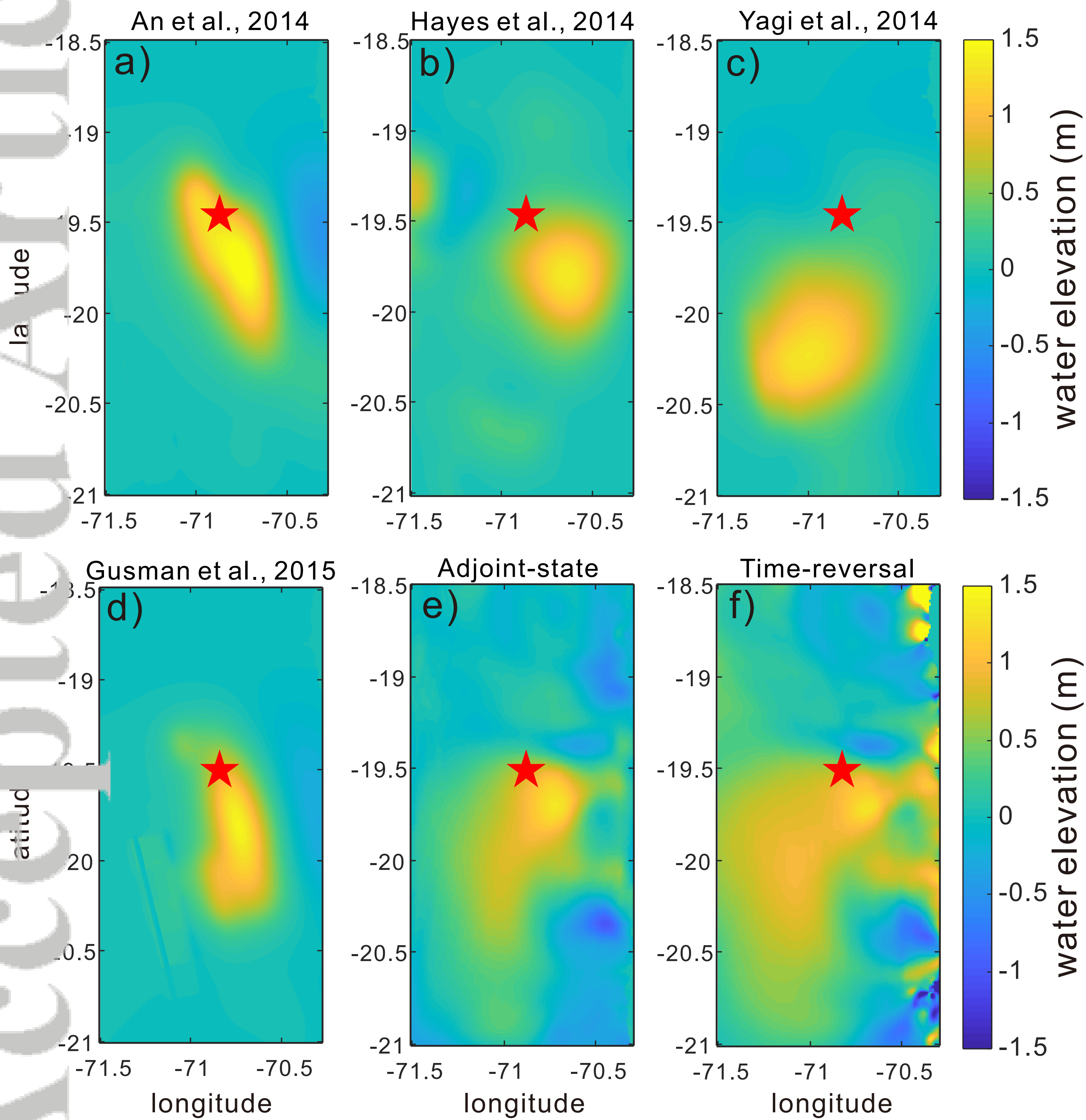
An et al., 2014
a)
Hayes et al., 2014
b)
Yagi et al., 2014
c)
Gusman et al., 2015
d)
Adjoint-state
e)
Time-reversal
f)
-18.5
-19
-19.5
-20
-20.5
-21
-71.5
-71
-70.5
longitude
1.5
1
0.5
0
-0.5
-1
-1.5
water elevation (m)